Experimental assessment of the performance of open joint ventilated façades with buoyancy-driven airflow

M.N. Sánchez [a], C. Sanjuan [a], M. J. Suárez [b], M.R. Heras [a],*

[a] *Department of Energy, Energy Efficiency in Buildings Unit, CIEMAT, 28040 Madrid, Spain*
[b] *Universidad de Oviedo, EDZE (Energía), Campus de Viesques, 33271 Gijón (Asturias) Spain*

[*]Corresponding author. Tel.: +34 914962515.
E-mail address: nuria.sanchez@ciemat.es (M.N. Sánchez).

Abstract

The relevance of a good design in the improvement of the thermal performance of a building turns especially critical in the façades, where some of the most significant heat exchanges between building and environment take place. The open joint ventilated façade (OJVF) is a construction system widely employed as an element of protection against the solar radiation, so a good characterization of the natural convection phenomena is required. This research focuses on the study of the thermal and fluid dynamic behavior of this construction system, paying particular attention to the description of the fluid turbulent structures induced by the solar radiation. With this purpose, five experiments have been performed corresponding to five simulated solar radiation incident on the surface of the façade, and no wind. These cases of study correspond to the following Rayleigh numbers: 1.52×10^9, 1.02×10^9, 5.94×10^8, 4.30×10^8 and 4.12×10^8. The laboratory façade model tested is a panel structure of 0.825 m high and 0.3 m wide composed of four panels and five corresponding horizontal joints of 5 mm. The air cavity is 40 mm wide. The velocity fields were obtained using the Particle Image Velocimetry (PIV) technique. These experiments have allowed the analysis of the fluid and thermal characteristics of the air flow inside the ventilated cavity, in the different conditions investigated, and to obtain a good description of the natural convection phenomena induced by the solar radiation. Results show that an ascending flow is produced inside the air cavity with a similar flow pattern regardless of the solar radiation incident on the façade.

Keywords: *Ventilated façades; Buoyancy driven flow; PIV measurements.*

1. Introduction

Currently, different active and passive techniques are being implemented in the design and construction of buildings increasing their energy efficiency by reducing their energy consumption. This reduction of the energy used in thermal conditioning of buildings contributes lowering CO2 emissions from buildings, reducing their impact on cli- mate change. Most of the passives strategies used, such as natural ventilated façade techniques, the use of shading devices or a proper external insulation, are based on actuations over the façade component of a building. The decisions on the façade design are of special relevance, because some of the most significant heat exchanges between building and environment take place in them. Active intelligent double skin façade, those with phase change material or with open joint ventilated are some of the different ventilated façades techniques which are currently under investigation and development.

This paper focuses on the study of open joint ventilated façades (OJVFs); a solution that combines technical and esthetic benefits, and which has been widely implemented in Mediterranean climates during the past years. This term refers to a construction system composed, from interior to exterior, of a mass wall with insulation on the exterior side, followed by an air cavity and an outer cladding made of opaque panels fixed to the vertical profile structure. The term “open joint” comes from the joints between the panels, which configure an ascending ventilation flow in the cavity rather different from other ventilated façades, see Fig. 1.

The existing scientific literature about the fluid and thermal behavior of OJVF is still quite limited. In previous works a 2.4 m high ventilated façade composed of four panels and their joints has been simulated and compared it to a conventional façade with sealed cavity (González et al., 2008a,b; Sanjuan et al., 2011c). Temperature fields, velocity profiles and heat fluxes transferred to the room were analyzed and discussed. Temperatures in OJVF are lower than temperatures in conventional façades with sealed cavity, considering a same incident solar radiation on the external cladding. That means less heat is transferred to the room.

The authors also provided a methodology to quantify the energy savings produced by OJVF and compared the results with simplified models of a ventilated cavity used in energy simulation software of buildings (Energy Plus).

Following the same methodology, a 2.4 m high ventilated façade composed of nine panels and ten horizontal joints has been simulated and compared its thermal and fluid behavior to a top and bottom ventilated façade with opaque outer layer and to a conventional façade (Millar et al., 2010). Under radiation conditions, the best behavior was shown by the OJVF, followed by the top and bottom ventilated façade, and finally by the conventional façade.

Apart from the above mentioned numerical studies, only two additional references related to experimental investigations on real OJVF can be found. During 2010, temperature, radiation, and velocity measurements were performed in a ventilated façade of a test building with a squared base of 2.89 m^2 and a total height of 7.75 m with a 24 cm air cavity (Marinosci et al., 2011). The modeling of the façade was made using the software ESP-r and three different air flow nodal network models were tested. The differences of the models depended on whether the joints along the façade were considered sealed or opened. Good agreement between

experimental and numerical temperature data was shown when considering the open joints in the modeling. However, the authors remarked that the air velocity measurements did not report any substantial information, and could not conclude anything. In a similar way, a real OJVF with a south oriented façade and a total height of 4.95 m was analyzed (Giancola, 2010). During the monitoring phase, the following variables were measured on the façade at different heights: surface and air temperature, heat fluxes to the building, and air velocity. Along with the façades sensors, ambient temperature, humidity, incident radiation on the façade, and direction and wind speed were also registered. The experimental results were compared to numerical simulations based on existing models (González et al., 2008a,b). Good coincidence between numerical and experimental temperature data was found when the numerical model considered the reflected radiation from the ground. However, in both studies, the comparison of the air velocities in the ventilated cavity did not allow obtaining an acceptable description of the flow.

Recently, velocity (PIV) and temperature measurements in a laboratory model of an OJVF were performed (Sanjuan et al., 2011a). The authors used an experimental unit consisting on a ventilated façade 0.825 m high and 0.3 m wide designed and built in order to study the convection in the interior of the ventilated cavity. Three experiments were carried out for different heating conditions – equivalent to different solar radiation values – and corresponding to the following Rayleigh numbers: $1.35x10^9$, $9.19x10^8$ and $5.92x10^8$. The authors reported detailed information of the mean flow behavior inside of the air cavity, paying special attention to the distribution of the flow through the joints. These experimental temperature and velocity results were compared to CFD simulations, obtaining a good agreement in the mean flow description (Sanjuan et al., 2011b).

The objective of this article is to describe the turbulent flow in the interior of the ventilated cavity in the open joint ventilated façades. This article presents the results of five additional experiments performed in an existing OJVF model (Sanjuan et al., 2011a). Based on this set up, different experiments were carried out using micronized oil as tracer particles. They correspond to the following Rayleigh numbers: $1.52x10^9$, $1.02x10^9$, $5.94x10^8$, $4.30x10^8$ and $4.12x10^8$. The results from the different experiments have been used to examine how the heating conditions influence the turbulent structures along the cavity. The instantaneous flow behavior and the time averaged flow structures are analyzed. Measurements are presented as contours of velocity and turbulence, and as horizontal profiles of averaged velocity and turbulence quantities.

2. Experimental set up

2.1. Description of the OJVF laboratory model and the PIV system

An experimental unit has been designed and built in order to study the natural convection in the interior of the cavity of an open joint ventilated façade. Specific dimensions and materials most frequently used in ventilated facades have been considered in the model design. One of the materials of tiles most extensive on the market is the ceramic, but also metallic or stone materials are used. The metallic material has been chosen for the model because of its lower thermal inertia, so less time was required to reach steady conditions at the experiments. Nevertheless, the model has not been designed maintaining a real façade structure but taking into account two technical considerations:

- The model has been adapted, due to the visual access requirements of PIV technique, by replacing the internal layers (wall mass and thermal insulation) by a glass surface.
- The height was limited to approximately half of the representative height between window panes in two consecutive floors.

All other characteristic dimensions of the model façade are based on existing components with joints less than 10 mm wide and cavities more than 30 mm wide. The height was limited in order to reduce the number of runs to complete one experiment. Numerical simulations of the flow behavior for OJVF with a representative height of 2.4 m (between window panes in two consecutive floors) have been recently developed by (Sanjuan et al., 2011b and Marinosci et al., 2011). Results determine a similar flow structure regardless of the different facade composition: five versus nine panels. A same fluid pattern has been found for the simulations and this assumption has been extended to this study. On this basis, the height of the façade model has been reduced to the half of the representative height. Experimental results obtained at the present study also reproduce the same fluid pattern where the ascending flow enters the air cavity through the lower joints while leaving through the upper joints. The flow through the central joints is negligible.

Details of the laboratory model are divided into three main parts:

- A ‘seeding box’; where the seeding is prepared and homogenized. The term “seeding” refers to the tracer particles transported by the fluid of study. The PIV technique is based on the measurement of the displacement of those particles in a period of time to characterize the fluid. According to this, the main characteristic of the seeding is to not change the properties of the fluid or its trajectory. The air inside the seeding box has the ambient pressure, so it allows to simulate exterior conditions corresponding to calm wind, and let the buoyancy forces (produced by the heating of the panels) force the circulation through the ventilated cavity.
- To minimize the number of spurious velocity vectors (vectors obtained from the PIV process that have incorrect values), appropriate number of seeding particles should be supplied to each interrogation area. It is desirable that tracer particles should be non-toxic, non-corrosive, non-volatile, non-abrasive and chemically inert. A wide variety of tracer particles is available for PIV experiments. Polyamide seeding particles have been used in many applications.
- Four metallic panels vertically disposed and separated by 5 mm horizontal joints. The panels simulate the outer cladding of a ventilated façade. Auto-adhesive electrical heating mats are placed on the external surface of the panels, with same

dimensions, in order to simulate the solar radiation. Each mat gets the same heating power as they are fed by a unique power source and connected on a parallel configuration. The panels are fixed at the front open side of the seeding box, as shown in Fig. 2.

- A 'cavity box' has been fixed at the front open side of the seeding box. This box forms an enclosure around the panels simulating the ventilated cavity. Some sur- faces are made of glass to let the laser light access into the cavity, forming the object plane, and to let the CCD camera capture images at this plane.

The x-distances have been normalized by the cavity width (W = 40 mm) and the y-distances have been normalized by the height of the cavity (H = 825 mm). x/W = 1 correspond to the heated panels. And y/H = 1 corresponds to the top of the cavity. More details on the OJVF model can be found in Table 1. Additional information about the experimental set up can also be consulted in previous articles (Sanjuan et al., 2011a).

The PIV system (from TSI) used in the present study consists of a double cavity Nd:YAG pulsed laser, a CCD camera connected to a PC and a Laser Pulse Synchronizer that automates the control of laser pulses and images registration, timing to external signals. Insight 3G Software was used to rule the system. Seeding was generated with a six jet atomizer which micronizes oil. Table 2 summarizes the PIV system parameters of the experimentation.

2.2. Velocity and temperature measurements

Velocity measurements were performed for the vertical centerplane of the cavity using the PIV system. Eight 'runs' were required because the height of the active area of the CCD camera in the experimental configuration is smaller than the whole height of the air cavity. Vertical dimension of the active area of the camera was 16.05 mm equivalent to 176 mm height at the real object plane. The height of the laboratory model is 825 mm so more than one run is required. The space has been discretized assuring that principal structures (i.e. vortex) of the flow are registered at the same run of images. This condition results in a total number of eight runs for each experiment. For each run, the laser and the cameras were displaced 10 cm in the vertical direction and 300 snapshots were recorded with a frequency of 7 Hz.

The displacement vectors were computed using the standard cross correlation with a 25% overlap of the interrogation regions. For each snapshot picture, the processing interrogation window has been set equal to 40 x 40 pixels that result in a spatial resolution of 2.3 mm x 2.3 mm of the velocity field in the measurement plane. Further postprocessing was made for rejected vectors occurred in areas of the image map where the seeding was too low or saturated pixels. This post processing of the snapshot data included a filter to remove bad vectors and the filling of the holes by interpolating from surrounding valid vectors.

To complement the PIV velocity measurements, temperature sensors have been placed in the center of each of the heated panels surface, and in the center of the air channel at the height of joints. Also, temperatures in the interior of the box where the seeding is prepared, and the laboratory temperature were monitored during each experiment. All temperature sensors used were PT100 class 1/10 DIN and 4-wire connection, meaning that the error in measure is below 0.1 °C. Their operating range between -20 and 70 °C meets our experiment requirements. The data acquisition used was the expandable system Compact FieldPoint Data logger which I/O modules where connected to a computer through the Ethernet port. A developed application written in LabView has been used to register the measurements each 30 s.

2.3. Seeding material

The tracer particles were nebulized by a six jet atomizer. The seeding material was olive oil and the diameter of the particles generated was approximately 1 μm. The Stokes number, St, is a measure of particle inertia and represents the ratio of the particle response time to characteristic flow timescale. As St → 0, the particles and fluid trajectories are equivalent. The Stokes number has been calculated according to the following formula:

$St = \rho_p \, d_p^2 \, U \, C_c / 18 \, \mu \, L$

where ρ_p is particle density, d_p particle diameter, U a characteristic velocity scale of the flow, C_c a slip correction factor, μ the fluid viscosity, and L a characteristic length scale of the flow. C_c has been set to 1.17 for 1 μm oil particles according to (Hinds, 1982). The values of the Stokes numbers for the experiments are in the range of 10^{-6} and indicate that the particles follow the fluid flow.

3. Study description

3.1. Experimental conditions

According to this experimental set up, five experiments were performed. Table 3 summarizes the heating conditions of them.

In one hand, the conditions of Experiment 1 can be considered as an upper limit in the temperatures reached in the building façades. These conditions correspond to an absorbed solar radiation of 525 W/m^2. Considering a value of 0.7 as the absorption in the exterior surface of the façades, this corresponds to a solar incident radiation on the façade of 750 W/m^2. On the other hand Experiment 5 has been set as the lower limit with an absorbed solar radiation of 80 W/m^2 corresponding to an incident solar radiation of 115 W/m^2. The reason of testing at a wide range of simulated solar radiations was to check if there were changes in the fluid structure.

3.2. Data analysis

Each experiment is completed after eight runs where consecutive regions of the cavity are measured. The time-averaged velocity vector field for each run has been calculated. The flow along the ventilated façade has been reconstructed taking into consideration the different flow structures which determine the velocity vectors fringe selected in each region. However not all instantaneous vector maps have been used for computing the mean flow. Time cross correlation between 300 instantaneous vector maps indicated the snapshots that differ from the mean flow. Snapshots with correlation factors lower that 99% were not considered in the mean flow calculation.

The instantaneous velocity fields have also been used to calculate the turbulence derivatives, such as the turbulence level (T_u), the turbulence intensity (I_t), the Reynolds Stresses (τ_{Re}) and the Turbulence Production (P). The x-distances have been normalized by the cavity width (W = 40 mm) and the y-distances have been normalized by the height of the cavity (H = 825 mm). x/W = 1 correspond to the heated slabs. And y/H = 1 corresponds to the top of the cavity.

The instantaneous velocity is composed of a mean part ($\bar{u}$) and a fluctuation part (u_i'), as it is expressed in the following equation:

$$u_i(x,y) = \bar{u}(x,y) + u_i'(x,y) \qquad (2)$$

The kinetic energy corresponding to the fluctuating components of the velocity is called turbulent kinetic energy (K), and it has been calculated according to the following equation:

$$K(x,y) = \frac{1}{2N}\sum_{i=1}^{N}\left[u_i'^2(x,y) + v_i'^2(x,y)\right] \qquad (3)$$

where N is the number of snapshots, u_i' is the fluctuating part of the x-component of the velocity and v_i' is the fluctuating part of the y-component of the velocity.

The turbulence (T_u) has been calculated according to the following equation:

$$T_u(x,y) = \sqrt{K(x,y)} \qquad (4)$$

This expression represents the absolute value of the time-averaged fluctuation of the velocity vectors. The turbulence intensity (I_t) has been calculated dividing the previous expression by the flow mean velocity. The turbulence intensity represents then the dimensionless level of fluctuation of the velocity in the following equation:

$$I_t(x,y) = \frac{\sqrt{K(x,y)}}{V(x,y)} \qquad (5)$$

where *V(x, y)* is the velocity magnitude computed from the mean flow velocity components *u(x, y)* and *v(x, y)*.

The Reynolds Stresses (τ_{Re}) have been calculated by Eq. (6). And if we attend to the sign of the Reynolds Stresses, the term of kinetic energy production (P) represents the work done by the Reynolds Stresses against the mean flow velocity gradients. This term has been calculated by Eq. (7):

$$\tau_{Re} = \frac{\langle u'v' \rangle}{V^2} \qquad (6)$$

$$P = -\langle u'v' \rangle \frac{\delta v}{\delta x} \qquad (7)$$

3.3. Error estimation

Errors in velocity vectors measurements with PIV technique can be divided into systematic and precision errors. The systematic errors are associated to the experimental model, mainly to the seeding quality and to the positioning of the measurements devices. As commented above, the seeding particles follow correctly the flow. Additionally, during the post processing, the bad vectors due to seeding inhomogeneities have been detected and replaced by interpolation. The positioning errors can be estimated in mm, and in any case, they do not have a direct influence in the velocity magnitude, but in its location. The precision errors can be calculated as the sum of an uncertainty component (U) and a stochastic component (S). For this work, the computation of the precision errors follows (Adeyinka and Neterer, 2004) studies. These authors express the fluid velocity for an interrogation window area at any instant as the following equation:

$$u = \frac{\Delta s L_o}{\Delta t L_i} \qquad (8)$$

where Δt is the camera timing, Δs is the particle displacement calculated through the correlation algorithm, L_o is the width of the camera view in the object plane, and L_i is the width of the digital image. The bias error of the fluid velocity is then related to the elementary bias errors of the velocity components as defined in the following equation:

$$U_u^2 = \eta_{\Delta s}^2 U_{\Delta s}^2 + \eta_{\Delta t}^2 U_{\Delta t}^2 + \eta_{Lo}^2 U_{Lo}^2 + \eta_{L_i}^2 U_{L_i}^2 \qquad (9)$$

where η_i are the sensitive coefficients and U_i are the elementary uncertainty errors.

According to the manufacturer (TSI), the uncertainty in the camera timing (Δt) is μs. L_o depends on the configuration and the respective distances between the laser plane (measurement plane) and the camera plane. Thus, its elemental uncertainty can be determined during the calibration of the PIV system. The calibration of the experiments is done by means of a calibration panel which consists on a matrix of white spots separated 10 mm between them. Each spot has a size of 1 mm. Based on these dimensions;

the maximum error during the manual calibration can be limited by half the size of the spot (0.5 mm). In the experiments, a distance of 234.795 mm in the measurement plane (laser plane) corresponds to 2048 pixel in the image plane. This allows us calculating an uncertainty of 0.875 pixels in the calculation of L_i.

Generally, the greatest source of uncertainty comes from the computation of the particle displacement Δs. Following (Bardera, 2005), mono-pulse images were taken in the same conditions as the experiments. After, a post processing of the image in Corel Photoshop was performed: the image was displaced 1 pixel, 3 pixels and 6 pixels. These images were combined with the first image to get three PIV double images (as if both lasers had been pulsed). The displacements were calculated with the PIV software. Table 4 shows the displacement values for the three cases.

Table 5 shows the computation of the resolution errors for the measured velocities in the five experiments.

The stochastic error (S) of the average velocities measured in the 300 snapshots is given by the following equation:

$$S = \frac{t\sigma}{N} \tag{10}$$

where t is equal to 2, σ is the standard deviation and N is the number of snapshots. An important part of this error is not really an "error", but a characteristic of the flow: the turbulence. However, this uncertainty can be considered as related to the calculation of the averaged velocity, but not to the instantaneous velocities.

Table 6 shows the mean precision errors for the five experiments.

The total uncertainty can be calculated by the root-sum-square method of both components (U and S). In the measured experiments, the value of the stochastic component is one order of magnitude below the uncertainty component (0.007 m/s). According to this, the relative uncertainty (divided by the magnitude of the velocity) with respect to the higher velocities is between 2% and 5% for the five experiments.

4. Results

The time averaged temperatures during the different experiments are represented in Fig. 3. The different curves show the surface temperatures of the panels and the air temperature inside of the ventilated cavity. Additionally to the PT-100 probes measurements, a thermographic camera has been used to measure the surface temperature of the panels (Fig. 4). The y-axis indicates the dimensionless position of the sensors.

The temperature tendencies show that the air inside of the cavity and the panels temperatures, increase with the height in the flow direction. These values confirm the "chimney effect" produced by natural convection. Although all the panels receive the same heating power, their surface temperature is not homogeneous because the flow through the joints cool the areas near the borders of the panels. The surface temperature is maximal at the center decreasing towards the edges. When the air enters the cavity through the lower joints it removes part of the heat from the lower panels. As the ventilation air ascends through the cavity, it increases its temperature, and the cooling potential decreases, for that reason the upper panels have higher temperatures. Still, the temperature inside the cavity is always lower than the panels. The temperature difference between the upper and the lower panel increases with the Rayleigh number.

4.1. Velocities

The following Fig. 5 shows the time averaged velocity vector maps in the centerplane of the cavity. The results show that the same fluid behavior and structures are observed in all the experiments. The air enters through the two lowest joints with a jet structure forming two recirculation vortexes near the heated panels. Once passed the recirculation vortex, the entering flow attaches to the heated panel and ascends through the cavity. In the central height of the air cavity, corresponding to a normalized y/H around 0.5, the flow rate is maximal as once passed the central height of the air cavity, the heated air starts to exit the cavity through the upper joints. The vertical component of the velocity, at this height, presents a homogeneous profile along the whole width of the cavity unlike what is observed at the high or low part of the façade, where lower velocities or even descending flow is detected near the mass wall. This behavior of the flow is related to the discontinuities at the joints.

However, the mean velocity of the flow increases with the heating conditions, and the higher velocities of the flow imply higher ventilation mass flow. In this figure it can also be observed that the dimensions of the turbulent structures (recirculation vortexes) also increase with the Rayleigh numbers.

Fig. 6 shows the horizontal profiles of the y-component of the velocity (Vy) for the dimensionless heights (y/H) corresponding to the center of the heated panels. The velocity profiles show that the ventilation flow does not maintain a homogeneous profile along the cavity. The velocity profiles corresponding to the first panel show that the flow, that entered the cavity with a jet structure, is still separated from the heated panels. The comparison of the different experiments shows that the jet structure is stronger for higher Ra numbers. In a similar way, the rounded profile in the region near the heated panels (x/W = 1), also shows that the flow at half height of the second panel has not jet reattached to the heated wall. On the contrary, the velocity profiles of the third and fourth panels evidence a flow that ascends the cavity attached to the heated panels, with a typical profile of convective flow between parallel plates of different temperature. The negative values near the cold wall imply the existence of inverse flow in certain regions of the cavity.

As commented above, the ventilation mass flow through the cavity increases with the Rayleigh number. Fig. 7 shows the mass flow through the joints measured for each experiment. The positive values indicate entering flow and negative values indicate outward flow. In general terms it can be concluded that around 50–60% of the total ventilation flow enters through the first joint (below), and the rest (40–50%) enters through the second joint. According to the measurements, the flow trough the central joint can be considered negligible. The ventilation flow exits the cavity through the upper joints, 40–50% through the fourth joint and the rest through the upper joint.

4.2. Turbulence

Figs. 8 and 9 show contours for the turbulence level (Tu) and for turbulence intensity (I_T) calculated according to formulas Eqs. (4) and (5). As it would be expected, the turbulence level (which quantifies the oscillation part of the velocity) increases with the mean flow velocity. However, the turbulence intensity, defined as the turbulence level normalized by the flow averaged velocity, is more similar in all the experiments compared to the similarities for the turbulence levels.

Fig. 10 shows the horizontal profiles of the turbulence production (P) calculated according to Eq. (6). The meaning of the term P can be understood by analogy with the viscous stresses that resist the deformation produced by the velocity gradients. The energy used to counteract the Reynolds Stresses is transformed in fluctuation movements. A negative production implies that the mean flow obtains energy from the turbulent fluctuations, while a positive production implies that the mean flow is adding energy to the turbulent fluctuations. According to this definition, the fluid near the heated panels (x/W = 1) adds energy to the mean flow, and this is how the horizontal part of the flow gets its energy. In the rest of the flow (cavity center and near the cold wall), the production term is positive, what means that the mean flow is transferring energy to the turbulent fluctuations, or said in other way, the turbulent fluctuations take energy from the mean flow.

4.3. Recirculation vortexes

The instantaneous velocity fields show that the flow can be considered steady and turbulent, including the oscillations in the vortexes formed inside the air cavity at the height corresponding to the first and second panels, at the low part of the façade. As commented above, these recirculation vortexes are produced due to the abrupt entrance of the flow inside of the cavity (jet structure), through the horizontal joints. At the first joint, the fluid enters the cavity with a main component which is horizontal, until it reaches the opposite (cold) wall. Gradually, the entering flow returns to the heated panel forming a recirculation vortex. At the second joint, the upstream flow from the lower part of the cavity, which enters through the first joint, modifies the jet structure reducing the size of the formed vortex.

The use of the laser in a "continuous" mode has allowed observing the oscillation of the vortexes. The following Fig. 11 shows the temporal evolution of the flow inside the air cavity at the height corresponding to the first panel. The consecutive images correspond to instantaneous velocity contours measured in continuous time steps. The velocity contours represent the vertical component of the velocity. The images sequence shows how the vortex con- tracts and expands, above all, in the vertical direction. It is also possible to observe some structures that separate from the mean jet flow that could be associated to small vortexes superposed to the jet flow.

A good way to visualize the oscillation of a fluid structure as a function of time is by calculating its centroid. Following the work of (Martínez-Suástegui and Treviño, 2008), the centroid of the fluid in the interior of a channel, with a main velocity component (y-velocity component in this case), can be defined in the following equation as:

$$X_u = \frac{\sum_{i=1}^{N} x_i v_i}{\sum_{i=1}^{N} v_i} \quad \text{and} \quad X_v = \frac{\sum_{i=1}^{N} y_i v_i}{\sum_{i=1}^{N} v_i} \tag{11}$$

where x_i represents the horizontal distance of each vector to the cold wall, and y_i represents the vertical distance of each vector to the cavity floor, v_i is the y-component of the velocity, and N is the total number of vectors in the analyzed region. The area in which the centroids have been calculated has been delimited by identifying closed velocity contours in the regions where the vortexes are expected. In this work, closed contours with a maximum velocity of 0.05 m/s have been used.

The analysis of the mean flow has allowed us to observe that the size of the vortexes increases with the Rayleigh number that characterizes the experiments. The instantaneous analysis also allows studying the oscillation amplitude of those vortexes. In this flow, the amplitude of the oscillation is directly related to the vortex size, which is at the same time related to the Rayleigh number. The higher the solar radiation incident on the surface of the façade, the bigger the vortexes are and thus, the more they oscillate.

The two small recirculation vortexes formed near the heated slabs at the entrance of the flow through the two lower joints have been studied, comparing the five experiments corresponding to the Rayleigh numbers: $1.52\text{x}10^9$, $1.02\text{x}10^9$, $5.94\text{x}10^8$, $4.30\text{x}10^8$ and $4.12\text{x}10^8$. A probability distribution of the centroid position, for the x and y components, of the recirculation vortexes formed in the air cavity have been calculated. The function represents the probability that the centroid positions is within a determined position interval. Figs. 12–15 represent these distribution functions for the x and y components of the centroid position for each vortex. The higher the Rayleigh numbers, the flatter and wider are the distribution functions of the centroid position. As the Ra number decreases, the functions form turns more narrow and skew. These data confirm the fact that the recirculation vortexes have more oscillation

amplitude for higher solar radiation, and for low radiation, these structures are much more stable, what traduces in less displacement along the cavity. The previous curves also show that as the temperature conditions increase, the centroid moves to the center of the cavity and upwards. This is a consequence of the increase of the dimensions.

5. Conclusions

This article reports an application of the particle image velocimetry (PIV) technique to characterize the velocity field and the turbulent structures inside the air cavity of open joint ventilated façades. The experimental design has been simplified because of the restrictions imposed by the measurement technique, but also because of the variety of commercial existing facades. The study has been limited to a specific type of ventilated facades characterized by having horizontal open joints and also the wind effect has not been considered. Although further analyses are required to complete the OJVF characterization, this initial study has allowed determining the main features of the air- flow inside the cavity leading to an increasing knowledge in OJVF characterization. They also serve as a benchmark to validate numerical models. Experiments for five different heating conditions corresponding to the following Rayleigh numbers: $1.52x10^9$, $1.02x10^9$, $5.94x10^8$, $4.30x10^8$ and $4.12x10^8$ have been performed. Main results are indicated in the following paragraphs.

The flow can be considered as steady under the conditions of the experiments. The observed fluid structures (jet flow, recirculation vortexes, flow separation and reattachment) indicate that the flow is turbulent. In general terms, the main flow is aligned with the cavity walls. The heating of the panels (solar radiation) produces, by natural convection, a ventilation flow that ascends the cavity with asymmetrical horizontal profile (higher velocities near the heated panels) and variable with the height marked by discontinuities in temperature, velocity and mass flow at the joints.

Same flow patterns repeat at the different experiments: the air enters the cavity through the lower panels (with a jet structure and forming a recirculation vortex), ascends through the cavity and leaves the cavity through the upper panels. The velocity and the turbulence of the flow increase with the temperature of the panels (number of Rayleigh of the experiments). Regarding the recirculation vortexes, the oscillation amplitude has been found to be related to the size of the vortex, which increases with the temperature of the panels.

Although further experimental work is required (three dimensional measurements, new experimental models including vertical joints, different height/width of the air cavity, wind conditions, etc.), the experimental work presented in this article can be considered as a first step in the investigation of the thermal and fluid behavior of open joint ventilated façade construction systems.

Acknowledgments

This research was done under the PSE-ARFRISOL Project (reference PSE-120000-2005-1). A scientific-technical research project of singular character, supported by the National Research, Development and Innovation Plan (Plan Nacional de I+D+I) 2004-2007 from the Spanish Education and Science Authority (Ministerio de Educación y Ciencia), funded with European Regional Development Funds (ERDF). The authors greatly thank all members of the PSE-ARFRISOL consortium for their support.

References

Adeyinka, O.B., Neterer, G.F., 2004. Experimental uncertainty of measured entropy production with pulsed laser PIV and planar laser induced fluorescence. International Journal of Heat and Mass Transfer 48, 1450–1461.

Bardera, R., 2005. Aplicación de PIV a la medida del coeficiente de resistencia aerodinámica, PhD. Thesis, Universidad Complutense de Madrid, Madrid, Spain.

Giancola, E., 2010. El comportamiento energético de una fachada ventilada de juntas abiertas, Tesis Doctoral, Universidad Politécnica de Madrid, Madrid, Spain.

González, M., Blanco, E., Pistono, J., 2008a. Adjusting an energy simulation model by means of CFD techniques to analyze open-joint ventilated façades energy performance. WREC-X 2008, Glasgow, Scotland.

González, M., Blanco, E., Río, J.L., Pistono, J., San Juan, C., 2008b. Numerical study on thermal and fluid dynamic behaviour of an open- joint ventilated faßcade. PLEA 2008, Dublin, Ireland.

Hinds, W.C., 1982. Aerosol Technology. John Wiley and Sons, New York, pp. 44–47, 407–408.

Marinosci, C., Strachan, P.A., Semprini, G., Morini, G.L., 2011. Empirical validation and modelling of a naturally ventilated rainscreen façade. Energy and Buildings 43, 853–863.

Martínez-Suástegui, L., Treviño, C., 2008. Transient laminar opposing mixed convection in a differentially and asymmetrically heated vertical channel of finite length. International Journal of Heat and Mass Transfer 51, 5991–6005.

Millar, I., Suárez, M.J., Blanco, E., Pistono, J., 2010. Análisis numérico del comportamiento térmico y fluidodinámico de una fachada ventilada de junta abierta. I Congreso sobre Arquitectura Bioclimática y Frío Solar 2010, Almería, Spain.

Sanjuan, C., Sánchez, M.N., Heras, M.R., Blanco, E., 2011a. Experimental analysis of natural convection in open joint ventilated facades with 2D PIV. Building and Environment 46, 2314–2325.

Sanjuan, C., Suárez, M.J., Blanco, E., Heras, M.R., 2011b. Development and experimental validation of a simulation model for open joint ventilated facades. Energy and Buildings 43, 3446–3456.

Sanjuan, C., Suárez, M.J., González, M., Pistono, J., Blanco, E., 2011c. Energy performance of an open-joint ventilated façade compared with a conventional sealed cavity façade. Solar Energy 85, 1851–1863.

Figures and Tables.

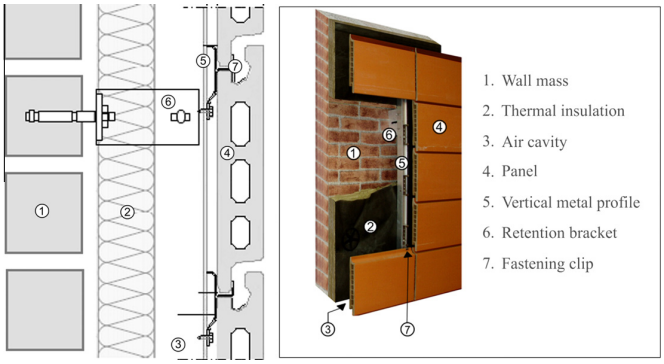

Fig. 1. Open joint ventilated façade. Construction detail.

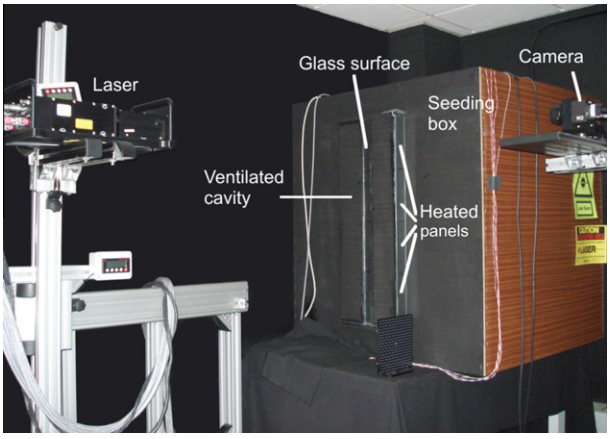

Fig. 2. OJVF laboratory model.

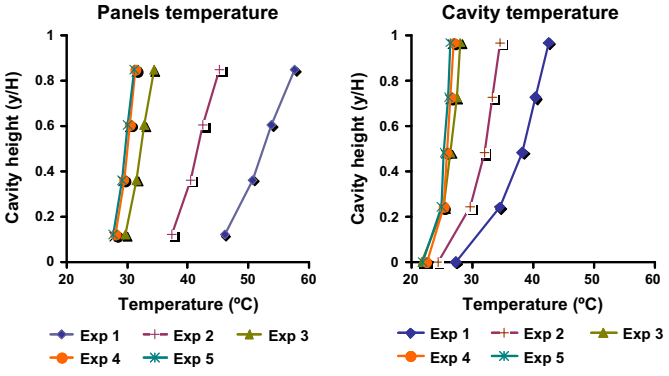

Fig. 3. Time averaged temperatures of the experiments. Exp 1 (Ra = $1.52x10^9$); Exp 2 (Ra = $1.02x10^9$); Exp 3 (Ra = $5.94x10^8$); Exp 4 (Ra=$4.30x10^8$); Exp 5 (Ra=$4.12x10^8$).

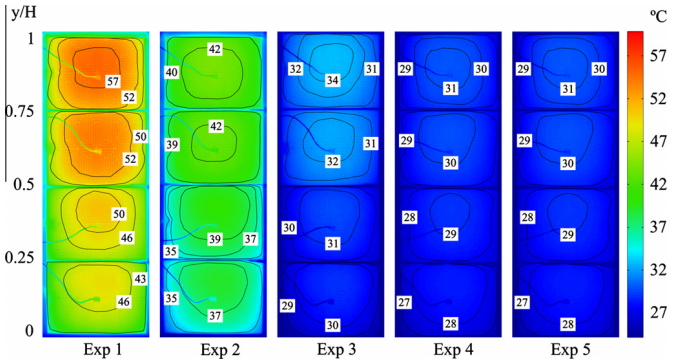

Fig. 4. Surface temperature of the heated panels. Exp 1 (Ra = $1.52x10^9$); Exp 2 (Ra = $1.02x10^9$); Exp 3 (Ra = $5.94x10^8$); Exp 4 (Ra=$4.30x10^8$); Exp 5 (Ra=$4.12x10^8$).

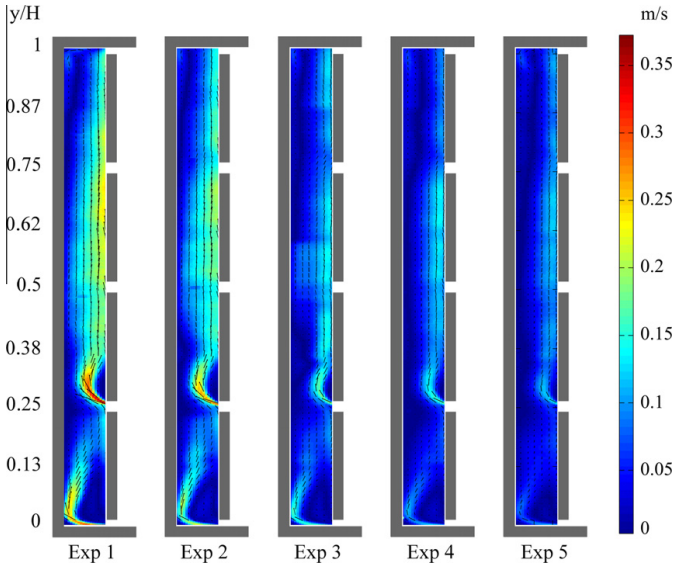

Fig. 5. Velocity vector maps. Exp 1 (Ra = $1.52x10^9$); Exp 2 (Ra = $1.02x10^9$); Exp 3 (Ra = $5.94x10^8$); Exp 4 (Ra=$4.30x10^8$); Exp 5 (Ra=$4.12x10^8$).

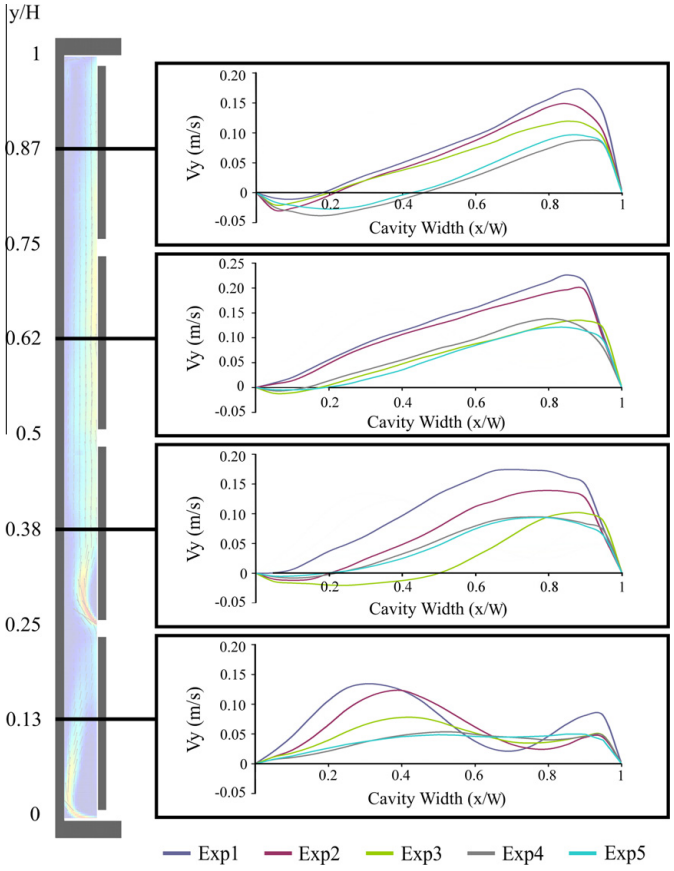

Fig. 6. Horiztonal profiles of the vertical component of the velocity. Exp 1 (Ra = $1.52x10^9$); Exp 2 (Ra = $1.02x10^9$); Exp 3 (Ra = $5.94x10^8$); Exp 4 (Ra=$4.30x10^8$); Exp 5 (Ra=$4.12x10^8$).

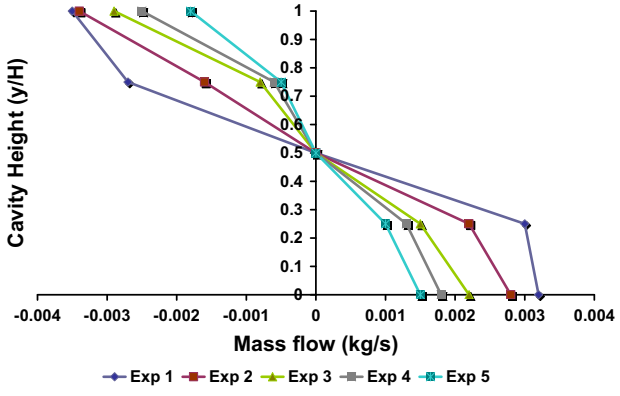

Fig. 7. Mass flow through the joints (kg/s). Exp 1 (Ra = $1.52x10^9$); Exp 2 (Ra = $1.02x10^9$); Exp 3 (Ra = $5.94x10^8$); Exp 4 (Ra=$4.30x10^8$); Exp 5 (Ra=$4.12x10^8$).

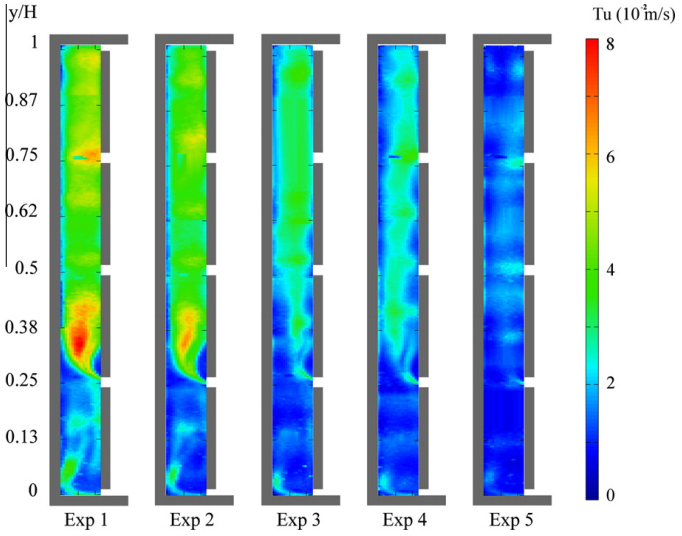

Fig. 8. Turbulence contours (Tu). Exp 1 (Ra = $1.52x10^9$); Exp 2 (Ra = $1.02x10^9$); Exp 3 (Ra = $5.94x10^8$); Exp 4 (Ra=$4.30x10^8$); Exp 5 (Ra=$4.12x10^8$).

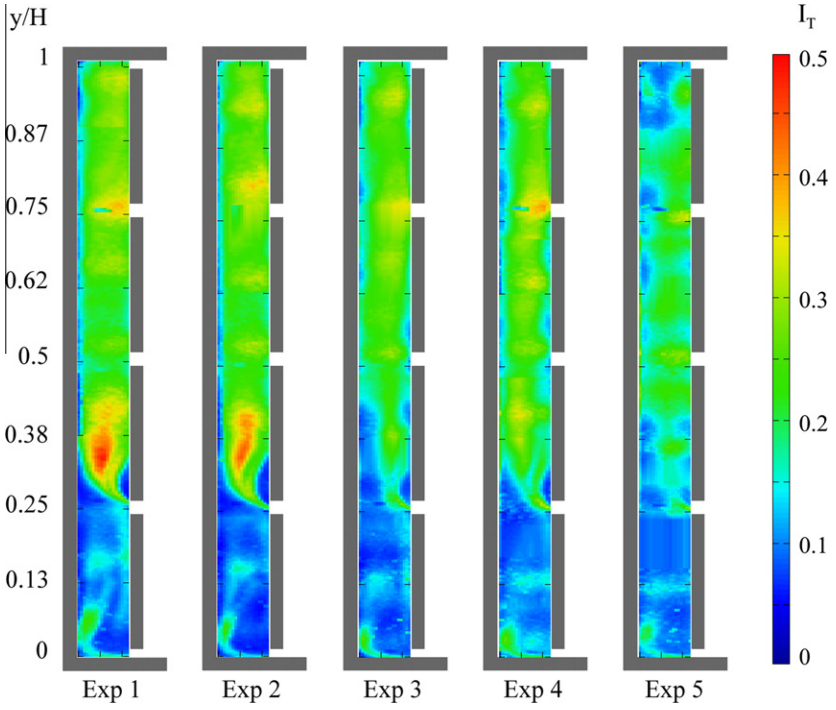

Fig. 9. Turbulence intensity contours (IT). Exp 1 (Ra = $1.52x10^9$); Exp 2 (Ra = $1.02x10^9$); Exp 3 (Ra = $5.94x10^8$); Exp 4 (Ra=$4.30x10^8$); Exp 5 (Ra=$4.12x10^8$).

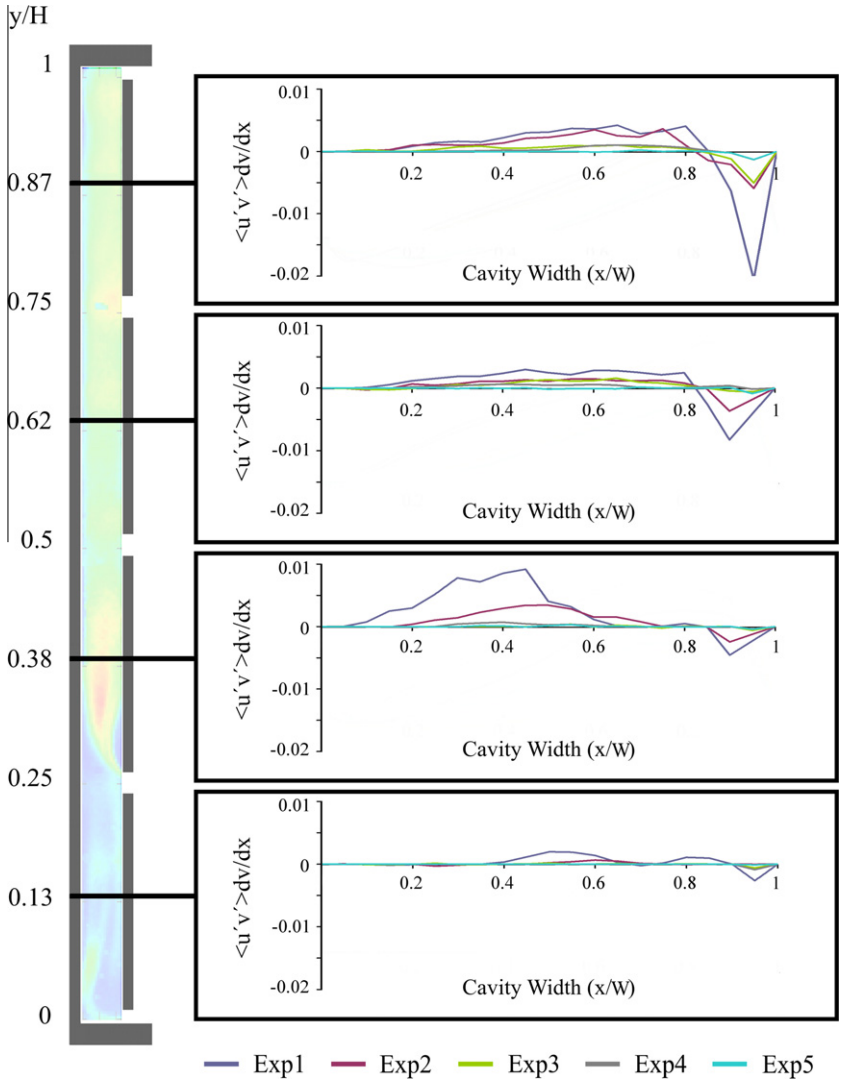

Fig. 10. Horizontal profiles of turbulence production (P). Exp 1 (Ra = 1.52×10^9); Exp 2 (Ra = 1.02×10^9); Exp 3 (Ra = 5.94×10^8); Exp 4 (Ra=4.30×10^8); Exp 5 (Ra=4.12×10^8).

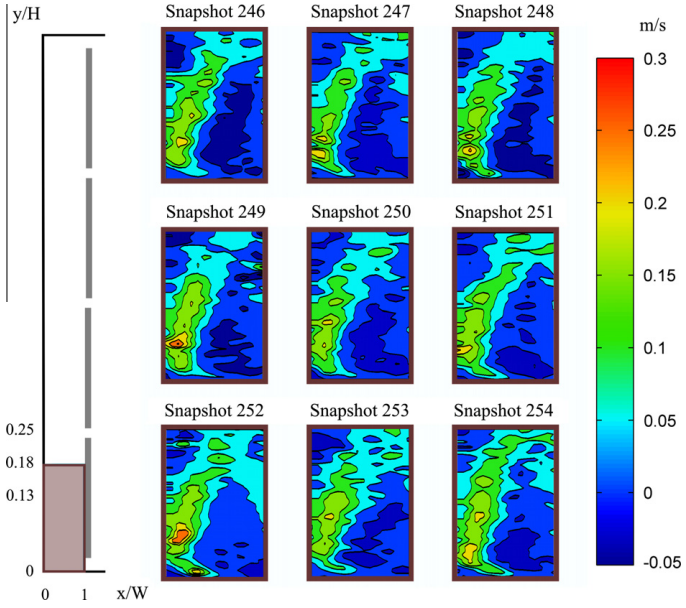

Fig. 11. Sequence of flow structures at a height corresponding to the lowest panel. Exp 1 Exp 1 (Ra = 1.52×10^9).

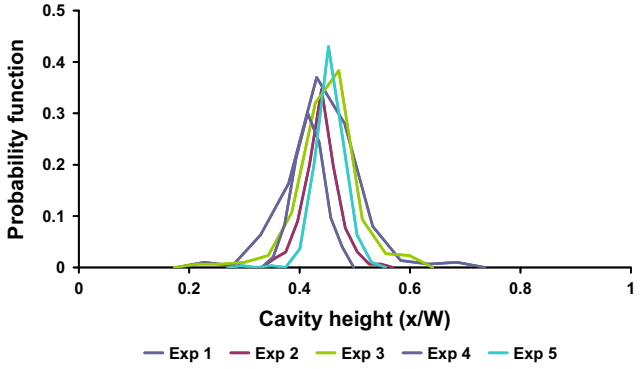

Fig. 12. Probability distribution function of the x-component of the centroid of the vortex formed at the height corresponding to the first tile.

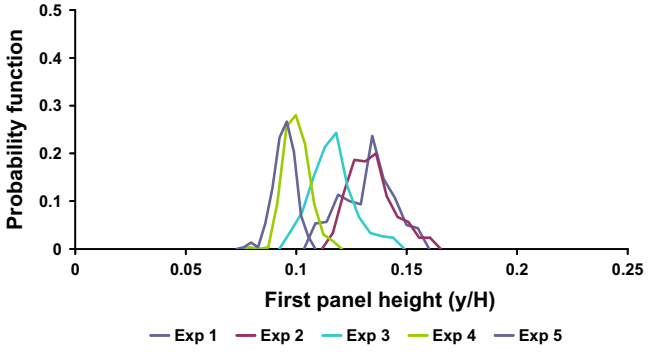

Fig. 13. Probability distribution function of the y-component of the centroid of the vortex formed at the height corresponding to the first tile..

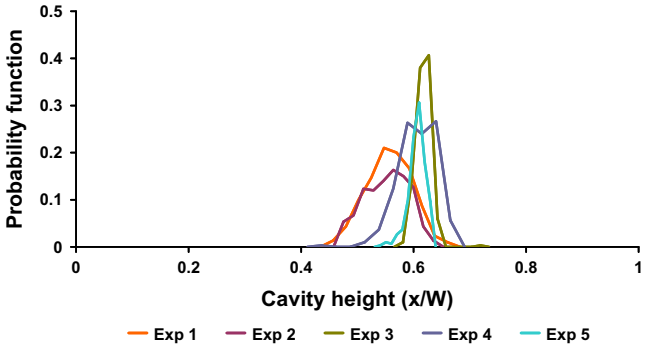

Fig. 14. Probability distribution function of the x-component of the centroid of the vortex formed at the height corresponding to the second tile.

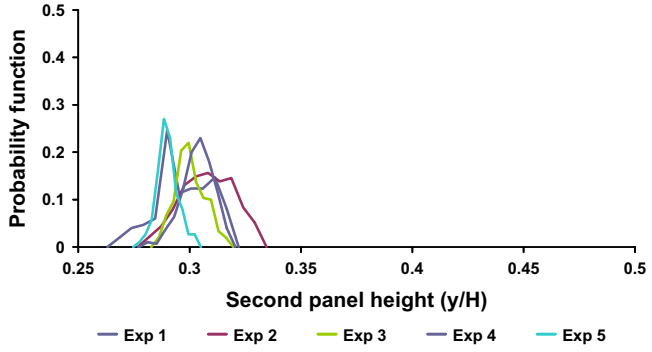

Fig. 15. Probability distribution function of the y-component of the centroid of the vortex formed at the height corresponding to the second tile.

Table 1
OJVF model description

Component	Quantity	Material	Dimensions (m)
Seeding box	1	Wood	$1 \times 1 \times 1$
Panels	4	Iron	$0.3 \times 0.2 \times 0.001$
Heating mats	4	Plastic	$0.3 \times 0.2 \times 0.001$
Ventilated cavity	1	Wood and glass	$0.3 \times 0.825 \times 0.04$

Table 2
Parameters of the PIV system experimental set up

Seeding	Six jet atomizer	
	Particle material	Olive oil
	Particle diameter	1 μm
Illumination	Laser	ND:YAG (YAG120-BSL)
	Wave length	532 nm
	Energy pulse	120 mJ
	Pulse repetition rate	15 Hz
	Time between pulses	100 ns
Camera	CCD	630,159 Power View 4MPlus
	Resolution	2048 × 2048 pixel
	Pixel	9.68
	Dynamic range	12bit
	Active area	16.67 cm × 16.05 cm
Images	Magnification (M)	11
	Maximum particle displacement	6 Pixel
PC	Frame grabber	16 frames/s Eight runs Snapshot frequency: 300 snapshots/run
Software insight 3G	Processing parameters	Standard cross correlation 25% overlap of interrogation windows Interrogation window: 40 × 40 pixel
2D Positioning structures	Displacement in vertical direction	Resolution 0.01 mm

Table 3
Heating conditions of the experiments

Heating conditions	Exp 1	Exp 2	Exp 3	Exp 4	Exp 5
Rayleigh number	1.52×10^9	1.02×10^9	5.94×10^8	4.30×10^8	4.12×10^8
Panels Heating power	35.1 W/mt	21.9 W/mt	11.85 W/mt	7.35 W/mt	4.82 W/mt
Simulated solar radiation	525 W/m^2	365 W/m^2	197 W/m^2	120 W/m^2	80 W/m^2
Averaged panels temperature	52.12 °C	41.41 °C	32.16 °C	39.88 °C	39.53 °C
Averaged seeding temperature	23 °C	22 °C	21 °C	22 °C	21.5 °C
Averaged temperature gradient in cavity	15.27 °C	10.33 °C	6.33 °C	4.53 °C	4.44 °C
Stokes number	1.79×10^{-5}	1.38×10^{-5}	9.78×10^{-6}	8.15×10^{-6}	8.15×10^{-6}

Table 4
Elementary resolution error for particle displacement

X_{real} (pixel)	1	3	6
$X_{measured}$ (mm)	1.14×10^{-1}	3.44×10^{-1}	6.89×10^{-1}
X_{real} (mm)	1.15×10^{-1}	3.45×10^{-1}	6.90×10^{-1}
Error (mm)	5.07×10^{-4}	5.37×10^{-4}	5.91×10^{-4}
Error (pixel)	4.41×10^{-3}	5.28×10^{-3}	5.15×10^{-3}

Table 5
Resolution error for the measured velocities

	Value	U_i	η_i	$U_i\eta_i$	$U_i^2\eta_i^2$	U
Lo (m)	0.235	10^{-4}	14.6	1.46×10^{-3}	2.15×10^{-6}	
Li (px)	2048	0.875	2048	0.875	0.00168	
Δt (s)	10^{-4}	10^{-7}	3.44×10^{-4}	3.44×10^{-3}	1.18×10^{-5}	
Δs (px)	3	0.00528	1.15	6.06×10^{-3}	3.67×10^{-5}	
Uncertainty					5.29×10^{-5}	0.007 m/s

Table 6
Stochastic error for the measured velocities

Uncertainty (%)	Exp 1	Exp 2	Exp 3	Exp 4	Exp 5
Region 1	2.9×10^{-4}	2.2×10^{-4}	3.7×10^{-4}	3.1×10^{-4}	1.3×10^{-4}
Region 2	3.5×10^{-4}	2.6×10^{-4}	2.1×10^{-4}	2.4×10^{-4}	1.9×10^{-4}
Region 3	5.0×10^{-4}	3.8×10^{-4}	3.5×10^{-4}	2.0×10^{-4}	2.6×10^{-4}
Region 4	3.9×10^{-4}	2.3×10^{-4}	1.8×10^{-4}	4.7×10^{-4}	1.8×10^{-4}
Region 5	5.9×10^{-4}	5.2×10^{-4}	2.9×10^{-4}	2.9×10^{-4}	4.2×10^{-4}
Region 6	3.7×10^{-4}	3.5×10^{-4}	2.2×10^{-4}	1.8×10^{-4}	2.6×10^{-4}
Region 7	3.3×10^{-4}	4.8×10^{-4}	3.4×10^{-4}	2.9×10^{-4}	3.1×10^{-4}
Region 8	4.1×10^{-4}	4.2×10^{-4}	3.7×10^{-4}	3.1×10^{-4}	2.8×10^{-4}
Average	4.04×10^{-4}	3.58×10^{-4}	2.91×10^{-4}	2.86×10^{-4}	2.54×10^{-4}